Journal of Materials Chemistry A

PAPER

View Article Online
View Journal | View Issue

Cite this: J. Mater. Chem. A, 2018, 6, 11252

Prediction of two-dimensional nodal-line semimetals in a carbon nitride covalent network†

Haiyuan Chen,[ab] Shunhong Zhang,[cb] Wei Jiang,[b] Chunxiao Zhang,[b] Heng Guo,[a] Zheng Liu,[cd] Zhiming Wang,[a] Feng Liu*[bd] and Xiaobin Niu*[a]

Received 19th March 2018
Accepted 30th April 2018

DOI: 10.1039/c8ta02555j

rsc.li/materials-a

Carbon nitride covalent compounds have emerged as a prominent member of 2D materials beyond graphene. The experimental realizations of 2D graphitic carbon nitride g-C_3N_4, nitrogenated holey graphene C_2N, and polyaniline C_3N have shown their promising potential in energy and environmental applications. In this work, we predict a new type of carbon nitride network with a C_9N_4 stoichiometry from first principles calculations. Unlike common C–N compounds and covalent organic frameworks (COFs), which are typically insulating, surprisingly C_9N_4 is found to be a 2D nodal-line semimetal. The nodal line in C_9N_4 forms a closed ring centered at the Γ point, which originates from the p_z orbitals of both C and N. The linear crossing occurs right at the Fermi level contributed by two sets of dispersive Kagome and Dirac bands, which is robust due to negligible spin–orbit coupling in C and N. Furthermore, it is revealed that the degeneracy along the high-symmetry path is protected by out-of-plane mirror or C_2 rotational symmetry, rather than in-plane mirror symmetry. The chemical potential difference between C and N, as validated by using a single orbital tight-binding model, plays a significant role in forming the nodal ring. Interestingly, a new structure of the nodal line, *i.e.*, a nodal cylinder, is found in momentum space for AA-stacked C_9N_4. Our results indicate possible functionalization for a novel metal-free C–N covalent network with interesting semimetallic properties.

Introduction

Graphene[1] discovered in 2004 has fostered a new research field of two-dimensional (2D) materials, attracting continued research attention. Much effort has been devoted to searching for new 2D materials beyond graphene. Next to C in the periodic table, N appears to be a suitable partner to compose another important set of 2D materials with C. 2D polyaniline with a C_3N stoichiometry has been successfully synthesized by a direct pyrolysis of hexaaminobenzene (HAB) trihydrochloride single crystals very recently.[2] The C_3N monolayer can be considered as *N*-substituted graphene with uniformly distributed N atoms in an ordered pattern, which possesses an indirect band gap.[3] This C–N compound has great potential not only for applications in nano-electronics but also as a functional unit.[4–6] In comparison with the hole-free honeycomb C_3N monolayer, holey generated C–N covalent networks[7–12] have also drawn a great deal of interest lately. Graphitic carbon nitride, g-C_3N_4, has been extensively studied for decades,[13,14] which crystallizes in a porous framework consisting of holes due to large N content.[7] Graphitic C_3N_4 has a direct band gap and can be potentially utilized in a wide range of energy and environmental applications, including fuel cells, catalysis, and gas production.[7–9] Likewise, nitrogenated holey graphene with a C_2N stoichiometry has been synthesized by a bottom-up wet-chemical reaction recently.[10] This 2D crystalline C_2N network, with regular holes, has a large electronic band gap of 1.96 eV, making it a promising candidate material for optoelectronics[10] and gas purification.[11,12] In addition, plenty of C–N materials with different C/N ratios have been theoretically designed *via* first principles calculations.[15–18]

So far, however, there has rarely been any investigation of 2D C–N covalent networks with metallic or better yet nodal-line semimetal (NLSM) features. NLSMs as new states of quantum matter have been intensively studied recently.[19–31] Particularly, C based Mackay–Terrones crystals (MTCs),[28] IrF_4 classes,[32] $PbTaSe_2$,[33] anti-perovskite Cu_3PdN,[26,30] and Ca_3P_2 (ref. 29) have been found to be 3D NLSMs. Attention has also been paid to 2D NLSMs with respect to both experimental research and theoretical design.[20–22,34–41] The experimental realization of 2D planar Cu_2Si[41] was reported to be a NLSM, in which the nodal lines form two concentric loops centered at the Γ point. However, the band touching in Cu_2Si is not rightly lying at the Fermi level and

[a]Institute of Fundamental and Frontier Sciences, School of Materials and Energy, University of Electronic Science and Technology of China, Chengdu 610054, P. R. China. E-mail: xbniu@uestc.edu.cn

[b]Department of Materials Science and Engineering, University of Utah, Salt Lake City, UT 84112, USA. E-mail: fliu@eng.utah.edu

[c]Institute for Advanced Study, Tsinghua University, Beijing 100084, P. R. China

[d]Collaborative Innovation Center of Quantum Matter, Beijing 100084, P. R. China

† Electronic supplementary information (ESI) available. See DOI: 10.1039/c8ta02555j

the existence of two nodal loops makes its experimental characterization more challenging. First-principles predicted that Hg_3As_2 (ref. 20) and PdS families[21] were only 2D NLSMs in the absence of spin–orbit coupling (SOC) but became gapped in the presence of SOC.[20,21]

In this work, we propose a novel covalent network consisting of C and N atoms with a C_9N_4 stoichiometry from first principles calculations. Most interestingly, it is found to be a 2D NLSM, in contrast to other chemically produced C–N compounds[2,3,7,10] as well as COFs[42,43] which are all insulating. The nodal line in C_9N_4 forms an ideal single loop centered at the Γ point without overlapping with any other bands in the momentum space. Mechanistically, this single loop is revealed to be the crossing of two separate sets of bands arising from two sub-lattices, namely the Kagome and Dirac bands. The interpenetration between Kagome and Dirac (honeycomb) lattices proposed recently can lead to different properties, like 2D topological insulators,[44,45] normal insulators,[46] half metals,[47] Dirac semimetals,[48] and 2D NLSMs.[20] In these materials, the sub-lattice sites were occupied by single atoms instead of molecular structural motifs, which is different from our case. The negligibly small SOC in C_9N_4 is significant for the robustness of the nodal line compared with the annihilation in other 2D NLSMs containing heavy metals.[20,21,40,41] Moreover, the large chemical potential difference between C and N plays a crucial role in the formation of the nodal line in C_9N_4, as further confirmed by charge transfer and tight-binding (TB) analysis. Interestingly, there is a new structure of the nodal line formed, *i.e.* a "nodal cylinder", in the whole Brillouin zone (BZ) along the k_z direction for AA-stacked C_9N_4. The gapless linear bands along the high-symmetry path are similar to those in graphene, which indicates higher electron mobility. Moreover, the planar 2D structure with a large surface-to-volume ratio affords plenty of chemically active sites, potentially useful in sensor applications.[49] Even in the bulk form with different stacking configurations, the system remains metallic, which is different from g-C_3N_4.[50] Similar to COFs, we propose a new graphene-type network in organic-conjugated polymer chemistry. Our results open an avenue for the design of both 2D NLSM and functional covalent organic frameworks.

Computational methods

The structural optimization and electronic band calculations are performed within the framework of density functional theory (DFT) using the Vienna *ab initio* simulation package.[51] The Perdew–Burke–Ernzerhof (PBE)[52] functional of generalized gradient approximation is employed. The projector-augmented wave[53] method is used to describe the ion–electron interactions. The HSE06 hybrid functional[54] is used to calculate the band structures to compare with the PBE results. The van der Waals interactions are included in the stacked structures by using a semiempirical DFT-D3 method.[55] The plane-wave energy cutoff is set to be 500 eV, and the energy convergence criterion in the self-consistency process is 10^{-6} eV. A 20 Å long slab layer is applied along the Z direction to avoid interactions between periodic images. A Γ centered 9×9 grid of k points is used to sample the BZ. The phonon spectrum is calculated using a 2×2 supercell with the Phonopy[56] code. *Ab initio* molecular dynamics (AIMD) simulations with an NVT ensemble are conducted to investigate the thermal stability of the C_9N_4 monolayer. The molecular properties are calculated using the Gaussian package[57] at the B3LYP level.

Results and discussion

As shown in the right panel of Fig. 1, the proposed covalent network has regular periodic nano-holes, in which C and N atoms are represented by black and blue balls, respectively. The hexagonal C rings in the network form a Kagome lattice, which is indicated by dashed green lines connecting each center of C rings, whereas the N constituents form a honeycomb lattice. Overall, C and N atoms share a 2D hexagonal lattice with the same crystal symmetry (D_{6h}) as graphene,[1] where the optimized lattice parameter is 9.64 Å. In the left panel of Fig. 1, a C ring joining with six N atoms is shown to form this new type of network. This building block is also the key component of the precursor HAB, which is utilized to synthesize crystalline C_3N[2] and C_2N[10] compounds. The unit cell of our proposed C–N network, indicated by red lines in Fig. 1, has 18 C atoms and 8 N atoms resulting in a C_9N_4 stoichiometry. It is worth noting that C_3N, C_2N, and C_9N_4 have very similar lattice geometries (Fig. S1 in the ESI†), indicating intimate structural relationships between these monolayer carbon nitrides. The C_2N unit cell is $\sqrt{3} \times \sqrt{3}$ times the C_3N unit cell by removing a C ring, while the C_9N_4 unit cell is twice the C_3N unit cell by removing another C ring. According to the atomic chemical environment and symmetry, there are two kinds of C and N atoms in C_9N_4. The optimized C–C and C–N bond lengths are similar to those in C_2N,[10] which indicates a strong covalency. The perforated covalent network has rich chemically active edge sites with a lone pair, suggesting its potential application in chemical sensors.

The uniformly distributed N atoms in the C_9N_4 network have an atomic size comparable with that of C and a five-electron valence structure, which makes it a favorable option to realize a strong covalent network. The C_9N_4 electronic band structure without SOC is shown in Fig. 2(a). There are two touching points denoted by D1 and D2 in the proximity of the Fermi level (set as

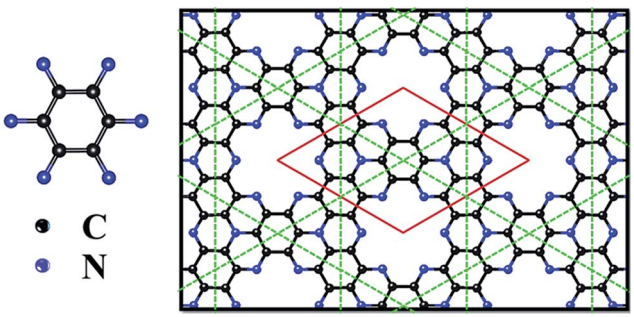

Fig. 1 The left panel shows the building block for the C_9N_4 covalent network. The right panel presents the C_9N_4 crystal structure, where the red line indicates the unit cell. The C rings form a Kagome lattice connected by green dashed lines.

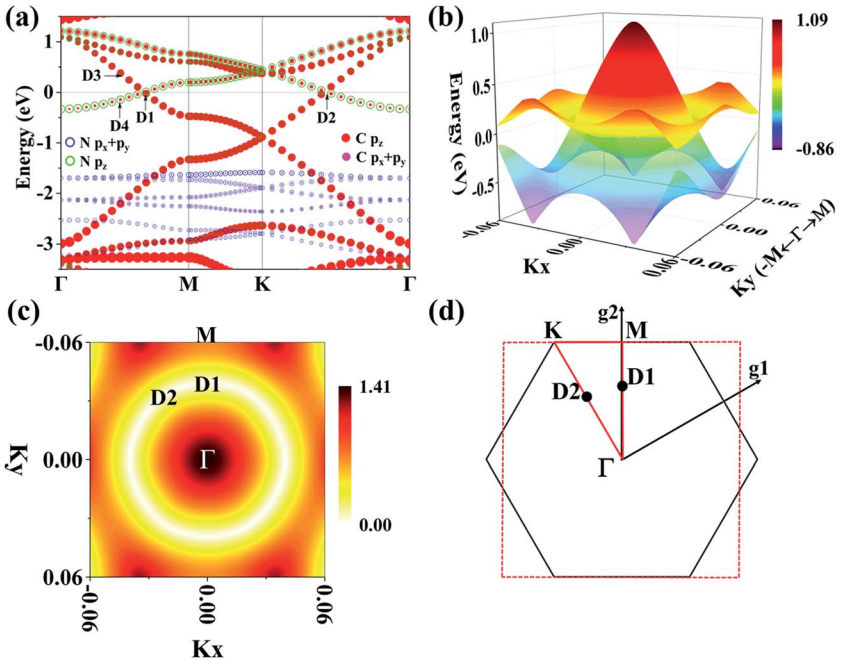

Fig. 2 (a) Projected band structure of C_9N_4, where the size of dots is proportional to the weight contributed by different orbitals. (b) 3D band structure of two crossing bands in the vicinity of the Fermi level around the Γ point. (c) 2D projected figure of the two crossing bands shown in (b), where the color bar indicates the energy difference between conduction and valence bands at each k point. (d) The 2D BZ of C_9N_4, where the dashed square is the projected area of (c).

zero), which indicates a semimetallic nature. This unusual feature is apparently different from those of most previously studied C–N compounds[2,3,7,10] and COFs,[42] which without exception are semiconducting or insulating. To reveal the origin of these two crossing points, the atomic-orbital resolved band structure is plotted in Fig. 2(a), where the sizes of the circles are proportional to the weight of related orbital contributions. It is clear that the two linear crossing bands near the Fermi level stem from the p_z orbitals of C and N atoms. The bands corresponding to the p_x and p_y orbitals lie much deeper below the Fermi level. Furthermore, there are two sets of distinguishable bands, the Kagome and Dirac bands. The former consists of one flat band and two dispersive bands, arising mainly from the p_z orbitals of C; the latter mainly arises from the p_z orbitals of both C and N, degenerating at K points. The two branches of the linear Kagome and Dirac bands cross each other at points D1 and D2 along Γ–M and Γ–K paths, respectively. To examine whether there are extra crossing points in the whole BZ, we calculated the band structures throughout the first BZ, as shown in Fig. 2(b). Clearly it shows that there are one concave and one convex energy surface crossing with each other around the Γ point, forming a single nodal loop in the BZ. Thus, we identify C_9N_4 to be a 2D NLSM. The crossing points D1 and D2 are two points in the same nodal ring as seen in Fig. 2(c). The projected square area of Fig. 2(c) in the first BZ is shown in Fig. 2(d) with red dashed lines.

We note that the gap is generally underestimated by standard DFT calculations, such as for g-C_3N_4 (ref. 14) and orthorhombic C_3N_4.[58,59] Therefore, to confirm the degeneracy of D1 and D2, hybrid functional calculations are conducted for C_9N_4 as shown in Fig. S2.† Clearly, the crossing points remain along Γ–M and Γ–K paths. On the other hand, bands from the p_x and p_y orbitals are located much deeper compared with the PBE results. Because the two crossing points are not high-symmetry points, we further calculated the bands around D1 and D2 using the HSE functional with a denser k-point mesh. As shown in Fig. S2(c–f),† the gap size around D1 and D2 remains essentially zero within the accuracy of numerical calculations, confirming the degeneracy of both D1 and D2.

To compare the states near the two crossing bands, we calculated the charge densities of states at points D3 and D4 close to D1 as shown in Fig. 3(a), which arise from the Kagome and Dirac bands, respectively. The D3 state mainly contributed by the p_z orbitals of C exhibits a Kagome distribution, as indicated by the green hexagons. It results from the C rings connecting with each other by an edge hopping path. As shown in Fig. 1, the eight N atoms in the unit cell form a 2 × 2

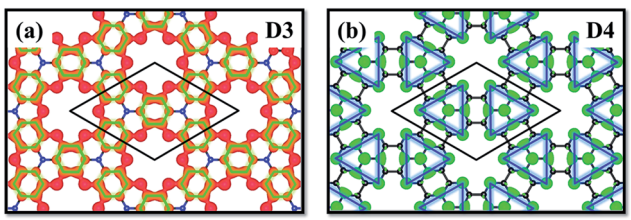

Fig. 3 Charge densities of (a) D3 and (b) D4 states decomposed from Kagome and Dirac bands close to the Fermi level, respectively. The green hexagons and blue triangles form Kagome and honeycomb lattices, respectively.

honeycomb sub-lattice; however, no band folding feature is observed in the band structure. Nevertheless, the Dirac bands cross at a high symmetry K point, indicating a bipartite "superlattice". For the D4 state, the Dirac bands can be considered as a super-honeycomb lattice consisting of two super-atoms in the unit cell labeled with the blue triangles displayed in Fig. 3(b). Each of the super-atoms has an identical atomic configuration with C_3 rotational symmetry without sharing common atoms. It is noted that the two sub-lattices in the Kagome–honeycomb composite lattice proposed before[20] is represented by single atoms instead of a bipartite "superlattice". Besides, the p_z (on the honeycomb sub-lattice) and s (on the Kagome sub-lattice) orbitals have opposite parities with respect to the in-plane mirror, which is different from the C_9N_4 lattice.

We note that the nodal line discovered in the previously reported 2D flat monolayer is protected by the in-plane mirror symmetry in the absence of SOC.[20,41] Meanwhile, the topological index $Z_2 = 0$ indicates that the nodal line in C_9N_4 is topologically trivial. In order to better understand the formation of degenerate points along the high-symmetry paths K–Γ and Γ–M, we analyze the group symmetry and parity of bands. The point group for 2D C_9N_4 is D_{6h}, so there are both one vertical mirror plane σ_v and one C_2 rotation axis existing along K–Γ and Γ–M as shown in Fig. 4(a and b). Along K–Γ and Γ–M, the k-points (except for the end points) from the two crossing bands have a C_{2v} point group, and the little group has both out-of-plane mirror σ_v and C_2 rotational symmetry along K–Γ and Γ–-M. As shown in Fig. 4(d), the two linear bands along K–Γ and Γ–M belong to two different 1D irreducible representations (A_2 and B_2). The two bands have opposite parities either with respect to σ_v or C_2 operation. Therefore, these two crossing bands along K–Γ and Γ–M are decoupled leading to two degenerate points, which are protected by the σ_v mirror or the C_2 rotational symmetry. Such degeneracy along high-symmetry paths is similar to the case of graphene,[60] and the main difference is that the touching points in 2D C_9N_4 are not at the high-symmetry points.

In addition, two more test calculations were carried out to artificially tune the planar structure to buckled structures to validate the role of σ_v mirror and C_2 rotational symmetries, as shown in Fig. S3(a and c).† The buckled structure in Fig. S3(a)† has the D_{3d} point group symmetry. Along K–Γ and Γ–M, the little group has σ_v mirror symmetry and C_2 operation, respectively. And the two crossing bands have opposite parities with respect to σ_v and C_2 along K–Γ and Γ–M, respectively, as shown in Fig. S3(b).† The buckled structure in Fig. S3(c)† has the C_{3v} point group symmetry. The corresponding band structure in Fig. S3(d)† clearly shows that there is only one degenerate point along Γ–M protected by σ_v mirror. However, the touching point is gapped along the K–Γ direction because both the σ_v mirror and the C_2 rotational symmetry vanish. The gap size (buckling height) is smaller (larger) in comparison with other 2D nodal-line materials containing metal atoms.[21] Interestingly, it is noticed that the degeneracy of Dirac bands at the K point increased due to the breaking of sub-lattice symmetry in the "bipartite" lattice, resulting in a sizeable gap E_D as shown in Fig. S3(d),† which is consistent with the chemical potential

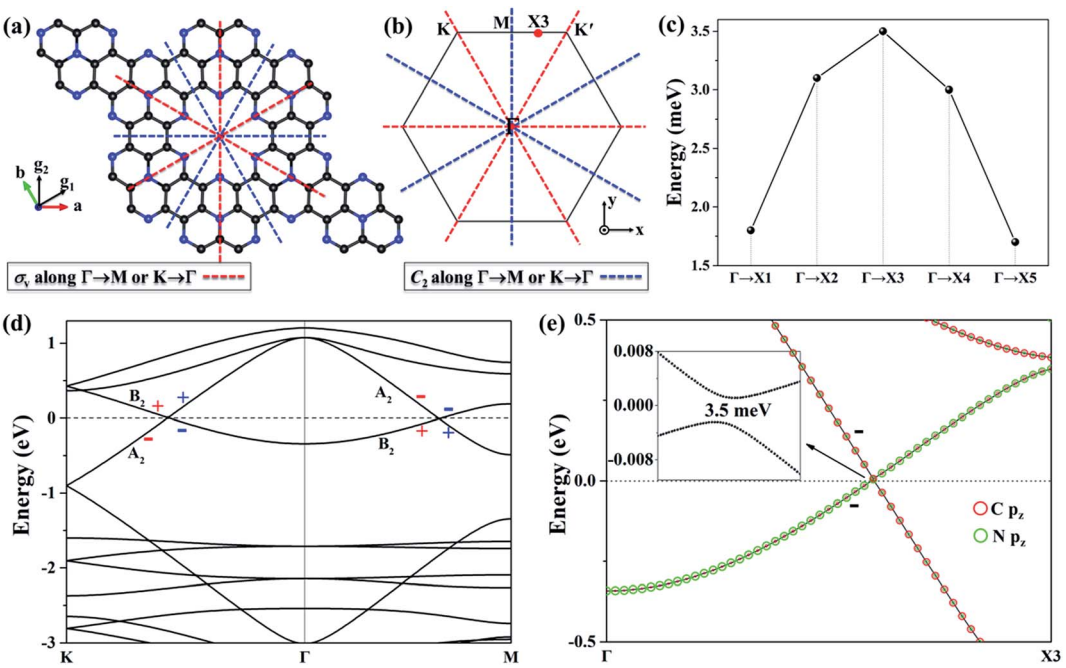

Fig. 4 (a) The 2D crystal structure and (b) BZ of C_9N_4, respectively, where the red and blue dashed lines indicate the out-of-plane σ_v mirror plane and C_2 rotation axis along K–Γ–M. (c) Gap size obtained along Γ–Xi (i = 1, 2, 3, 4, 5). (d) Band structure of C_9N_4 along K–Γ–M, where the "+" and "−" symbols indicate the parities of crossing bands with respect to the σ_v mirror plane or C_2 rotation axis in the same color. (e) Band structure of C_9N_4 along Γ–X3, where the "−" symbol indicates the parities of crossing bands with respect to the horizontal mirror plane. The green and red circles are proportional to the contributions from the p_z orbitals of N and C, respectively.

difference between the two super-atoms occupying the two sublattices, respectively.

In addition to the degeneracy along high-symmetry paths, we also examined other touching points in the nodal ring (Fig. 2(c)). The band structure shown in Fig. 4(e) is calculated along the Γ–X3 path. The point X3 is in the middle of the M–K′ path as shown in Fig. 4(b). The magnified band in Fig. 4(e) shows that there is a tiny gap (3.5 meV) opened at the nodal point along the Γ–X3 path, which can be understood by symmetry analysis. The *k*-points along Γ–X3 (except for the end points) have the C_s point group symmetry. The little group has one horizontal mirror plane σ_h. Because the crossing bands are all contributed by p_z orbitals, they become coupled with the same odd mirror parities with respect to σ_h. This gives rise to the as-formed tiny gap. Tiny gaps are also found along Γ–X*i* (i = 1, 2, 3, 4) as shown in Fig. 4(c). Their sizes are all checked within denser *k*-points calculated at the PBE level. The 5 X*i* (i = 1, 2, 3, 4, 5) *k*-points divide the M–K′ path equally. From Fig. 4(c), it is further seen that the gap sizes along the other four paths are symmetrical with respect to those along Γ–X3. Given the symmetry of *k*-points in the first BZ, it is known that there are in total 12 exact degenerate points in the nodal ring. The largest gap size is 3.5 meV along the nodal ring according to PBE calculations, which is confirmed to be in the same order of magnitude of about 3 meV by HSE calculations. Given this negligible gap size induced by weak coupling of p_z orbitals, the 2D C_9N_4 can still be considered as a NLSM.

The above calculations are performed without SOC, so it is natural to ask whether this nodal line in C_9N_4 is immune to SOC. It is found that the SOC strength (even artificially tuning larger) induced gap size is very tiny as shown in Fig. S4.† Hence, the nodal line in C_9N_4 is robust against the intrinsic SOC effect in C and N. Therefore, all three factors, the protection of multiple crystal symmetries, negligible SOC and negligible gap size induced by p_z-orbital coupling, contribute together to provide the 2D C_9N_4 with ideal semimetallic properties.

To better understand the effect of the chemical potential difference on the formation of the nodal loop in C_9N_4, a TB analysis is shown below. Due to the fact that only the p_z orbitals of both C and N atoms contribute to the states close to the Fermi level, we can construct a TB model with only the p_z orbitals,

$$\hat{H} = \sum_i \varepsilon_i a_i^+ a_i + \sum_{i \neq j} t_{ij} a_i^+ a_j \quad (1)$$

where a^+ and a are electron creation and annihilation operators, i and j are the sites of atoms in the unit cell, t_{ij} is the hopping energy between p_z orbitals at sites i and j, and ε is the on-site energy. We only consider the nearest-neighbor hopping without SOC. As mentioned above, there are two different C and N atoms according to the symmetry and chemical environment. Consequently, four interatomic hopping terms are introduced into the TB model, as shown in Fig. 5(a). The red and gray balls represent N and C atoms, respectively, whose size denotes the charge value based on the grid-dependent Bader charge analysis.[61] The calculated results indicate that each N(1) (N(2)) atom gains 1.1 (1.2) electrons, while each C(1) (C(2)) atom loses 0.6 (0.3) electrons. Apparently, the charge transfer occurs from C to N due to their electronegativity difference. The TB band structure is calculated to fit the DFT results as shown in Fig. 5(b), where only five bands comprising three Kagome and two Dirac bands are plotted. Table 1 lists the corresponding fitting parameters of hopping and on-site energies. The bond lengths between different atoms, for which the hopping integrals are indicated from t_1 to t_4 (Fig. 5(a)), are 1.39, 1.46, 1.42, and 1.34 Å, respectively. The hopping integrals are about the same since the bond lengths are close to each other. However, it is obvious that the on-site energy difference between C and N is rather large. Interestingly, we found that the superposition of

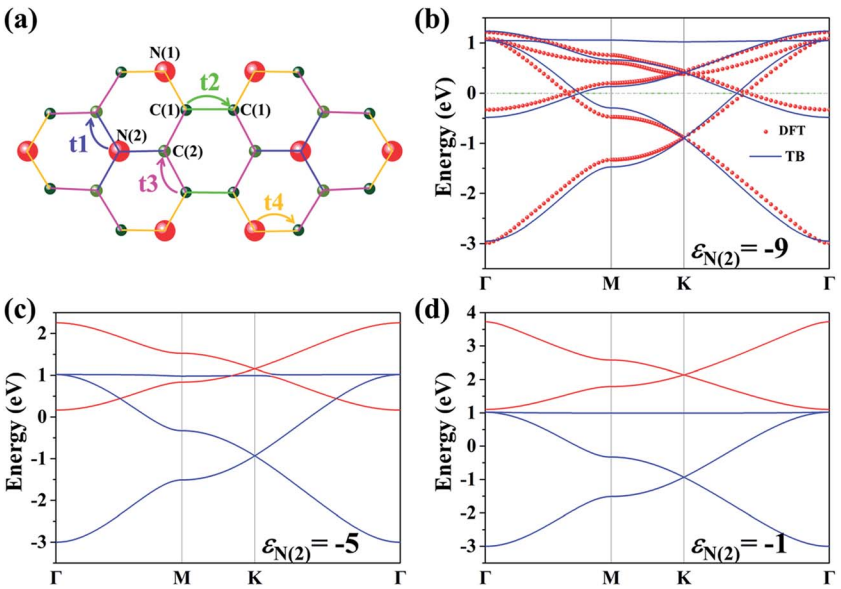

Fig. 5 (a) Bader charge analysis of the C_9N_4 unit cell. The red and gray balls represent N and C atoms. The sizes of balls indicate the charge values. (b) Band structure of C_9N_4 simulated by TB analysis (blue solid line) compared with the DFT results (red dashed line). (c) Band structure of C_9N_4 simulated by TB analysis with $\varepsilon_{N(2)} = -5$ eV and (d) $\varepsilon_{N(2)} = -1$ eV, while other parameters are fixed.

Table 1 Values of hopping and on-site energies (unit is electron-volt) applied in TB analysis

	t_1	t_2	t_3	t_4
p_zp_z	4.0	3.8	3.9	4.1
On-site energy	$\varepsilon_{N(1)} = -5$	$\varepsilon_{N(2)} = -9$	$\varepsilon_{C(1)} = 0.8$	$\varepsilon_{C(2)} = 0.0$

the three Kagome bands and the two Dirac bands is mainly attributed to the large on-site energy of N(2) atoms. As illustrated in Fig. 5(c and d), the Dirac point shifted upwards above the flat Kagome band when the on-site energy of N(2) atoms is decreased, while the other TB parameters are fixed. Moreover, the width and dispersion of the three Kagome bands are barely affected, and only the Dirac bands are influenced by the change of the on-site energy of two super-atoms in the unit cell. In particular, when the on-site energy of N(2) atoms changes to −1 eV, the linear band crossing disappears as shown in Fig. 5(d). Therefore, the linear crossing is mainly determined by the larger on-site energy of N(2) atoms. Also seen from Fig. 5(b), the band structures obtained by TB and DFT calculations agree well except for the flat band. From the DFT results (Fig. 2(a) and 5(b)), the flat band is pulled down to the *K* point and becomes slightly dispersive, which is different from the perfect flat band in the TB results. This is because in the TB calculations, only nearest-neighbor hopping terms are considered. In fact, such a localized flat band in the Kagome lattice is known to become dispersive when introducing second nearest neighbor hopping interactions.[62] Furthermore, in the DFT calculations, the linear-crossing bands are contributed by the p_z orbitals of both honeycomb and Kagome lattices. Hence, there are hybridizations between the Dirac and Kagome bands. Nevertheless the main feature of linear crossing pertaining to the two sets of dispersive bands is captured by the TB model.

To further understand the formation of the intrinsic nodal ring in our 2D covalent system, the properties of molecular orbitals (MOs) for a single super atom (C_9N_4) and whole unit cell ($(C_9N_4)_2$) are calculated with the Gaussian package. As seen from Fig. S5,† the unoccupied MOs from Dirac bands and partially filled MOs from Kagome bands determine the electron filling from the DFT results, *i.e.*, nearly unfilled Dirac bands and 2/3 filled Kagome bands. Moreover, the interaction between the wider dispersive Kagome bands and the narrower Dirac bands leads to a crossover giving rise to a degenerate nodal loop. More details are shown in the ESI.†

The relative energy stability among different stacking configurations is investigated. We started with the AA-stacking, which has an optimized interlayer length of 3.45 Å, typical of a van der Waals (vdW) interaction. As shown in the inset of Fig. S6(a),† the top layer is then shifted along one of the shorter diagonal directions until reaching half of the lattice constant of AA-C_9N_4 to assume an AB-stacking. The AB-stacking is found to be energetically more preferable by 38 meV per atom. This implies that the AA-stacking is metastable but may still be energetically accessible as seen in other 2D materials.

Due to the missing of some crystal symmetries along M–Γ–K in AB-stacked C_9N_4, some crossing points become gapped as shown in Fig. S6(b),† whereas they remain gapless along M–Γ–K in AA-stacked C_9N_4, in which the crystal symmetries are preserved as in 2D C_9N_4. We note that neither AA nor AB-stacked C_9N_4 is a semiconductor, which is different from the AA and AB-stacked g-C_3N_4.[50]

The band structure of AA-stacked C_9N_4 is shown in Fig. S7.† Interestingly, the two linear crossing points shift downwards from the $k_z = 0$ to the $k_z = 0.5$ plane. Therefore, the crossing points will form a new structure of the nodal line, *i.e.* a "nodal cylinder", along the k_z direction in the whole BZ, which is different from other simple nodal-line semimetals,[23,24,27,63,64] nodal-chain metals,[32] nodal-net semimetals,[26,30] nodal-link semimetals,[19,65,66] and nodal-knot semimetals.[67] As shown in Fig. S8,† there are two nodal lines along the k_z direction on the $k_y = 0$ plane, which further confirm the existence of the nodal cylinder. Therefore, the preserved crystal symmetry and weak vdW interactions ensure the existence of the nodal cylinder in AA-stacked C_9N_4.

Finally, to evaluate the stability of such a new type of C–N network, we compare the energy of monolayer C_9N_4 with those of pristine graphene and other experimentally realized 2D C–N materials (C_3N, C_2N, and g-C_3N_4). The lower energy shown in Fig. S9† for monolayer C_9N_4 partially confirms its higher stability. This result is in agreement with those of the previously studied 2D C_3N, C_2N, and g-C_3N_4.[4] However, such a comparison of total energy is insufficient because of their different stoichiometries. Therefore, we further calculate the formation energies of different C–N compounds using the chemical potentials from two known reagents, graphene and molecular nitrogen, according to the formula: $E_f = [E_{tot}(C_pN_q) - p/2 \times E_{tot}(\text{graphene}) - q/2 \times E_{tot}(N_2)]/(p + q)$, where p and q are the number of C and N atoms in the unit cell, respectively; $E_{tot}(C_pN_q)$, $E_{tot}(\text{graphene})$, and $E_{tot}(N_2)$ are the total energy of 2D C–N compounds, graphene, and N_2, respectively. The formation energies in Fig. S9† show similar trends to the total energies, suggesting the energetic stability of 2D C_9N_4.

Moreover, the phonon and AIMD computations are performed. There is no soft mode observed in the phonon spectrum (Fig. S10†), indicating its dynamic stability. Further calculations are conducted to study the thermal stability at room temperature (300 K) by performing AIMD simulations. The results (Fig. S10(b and c)†) indicate that there is no structural decomposition observed at 300 K after 10 ps. We also calculated the linear elastic properties from the strain-energy relationship using DFT calculations to investigate the mechanical stability. Due to symmetry, the 2D hexagonal crystal has two independent elastic constants C_{11} and C_{12}.[68] The computed values of C_{11} and C_{12} are 208 and 49 N m^{-1}, respectively, which fulfill the Born stability criteria[69] ($C_{11} > 0$, $C_{11} > |C_{12}|$). Other elastic quantities, such as Poisson's ratio and Young's moduli, can be evaluated using the following equations,[70,71]

$$v = \frac{C_{12}}{C_{11}}, \quad E = \frac{{C_{11}}^2 - {C_{12}}^2}{C_{11}} \tag{2}$$

The obtained in-plane Poisson's ratio (Young's moduli) is 0.24 (196 N m^{-1}), which is larger (smaller) than those of graphene and C_3N.[71] Therefore, our calculations of phonon

dispersion, AIMD simulations, and mechanical elastic properties consistently suggest that the C_9N_4 network has rather high thermodynamic and mechanical stabilities. All the evidence suggests that the synthesis of 2D C_9N_4 under ambient conditions is possible. We propose that C_9N_4 could be possibly synthesized utilizing similar synthesis processes applied for g-C_3N_4,[7] C_2N,[10,72] C_3N,[2,3] and COFs.[42]

Conclusions

In summary, a new 2D NLSM is predicted using first-principles calculations, which enriches the realm of both COFs and C–N compounds. This novel monolayer with a C_9N_4 stoichiometry possesses a nodal line centered at the Γ point in the k-space forming a closed loop. This new feature is rarely found in other C–N compounds and COFs. The touching points along K–Γ–M are protected by the out-of-plane mirror and C_2 rotational symmetry. The nodal line is contributed by the p_z orbitals of C and N, as further confirmed by a single orbital TB analysis. From the analysis on charge transfer and TB results, it is found that the C and N have a large on-site energy difference; particularly, the much larger on-site energy of N(2) atoms plays a significant role in forming such linear crossing at the Fermi level. The single nodal loop in C_9N_4 is intrinsically immune to the SOC effect due to the super light constituent elements, C and N, which shows ideal semimetallic properties compared with heavy metal-involved NLSMs. Interestingly, a nodal cylinder forms in the AA-stacked C_9N_4 along the k_z direction in the whole BZ. The thermodynamic and mechanical stabilities of 2D C_9N_4 are guaranteed by our calculations. Our results not only shed light on searching for a new kind of 2D C–N material, but also suggest a novel member among COFs with unusual semimetallic properties.

Conflicts of interest

There are no conflicts of interest to declare.

Acknowledgements

X. N. acknowledges the financial support from the Recruitment Program of Global Young Experts of China and Sichuan one thousand Talents Plan. F. L. acknowledges the support from the US-DOE (Grant No. DE-FG02-04ER46148). H.C. acknowledges the financial support from the Graduate School of UESTC. S. Z. is supported by the National Postdoctoral Program for Innovative Talents of China (BX201600091) and the funding from the China Postdoctoral Science Foundation (2017M610858). The computational resources are provided by the CHPC at the University of Utah and the National SuperComputer Center in Tianjing, China.

References

1 K. S. Novoselov, A. K. Geim, S. V. Morozov, D. Jiang, Y. Zhang, S. V. Dubonos, I. V. Grigorieva and A. A. Firsov, *Science*, 2004, **306**, 666–669.
2 J. Mahmood, E. K. Lee, M. Jung, D. Shin, H. J. Choi, J. M. Seo, S. M. Jung, D. Kim, F. Li, M. S. Lah, N. Park, H. J. Shin, J. H. Oh and J. B. Baek, *Proc. Natl. Acad. Sci. U. S. A*, 2016, **113**, 7414–7419.
3 S. W. Yang, W. Li, C. C. Ye, G. Wang, H. Tian, C. Zhu, P. He, G. Q. Ding, X. M. Xie, Y. Liu, Y. Lifshitz, S. T. Lee, Z. H. Kang and M. H. Jiang, *Adv. Mater.*, 2017, **29**, 1605625.
4 B. Mortazavi, *Carbon*, 2017, **118**, 25–34.
5 M. Makaremi, B. Mortazavi and C. V. Singh, *J. Phys. Chem. C*, 2017, **121**, 18575–18583.
6 W. F. Li, X. Dai, J. Morrone, G. Zhang and R. H. Zhou, *Nanoscale*, 2017, **9**, 12025–12031.
7 X. C. Wang, K. Maeda, A. Thomas, K. Takanabe, G. Xin, J. M. Carlsson, K. Domen and M. Antonietti, *Nat. Mater.*, 2009, **8**, 76–80.
8 Y. Zheng, J. Liu, J. Liang, M. Jaroniec and S. Z. Qiao, *Energy Environ. Sci.*, 2012, **5**, 6717–6731.
9 Y. Zheng, Y. Jiao, J. Chen, J. Liu, J. Liang, A. Du, W. M. Zhang, Z. H. Zhu, S. C. Smith, M. Jaroniec, G. Q. Lu and S. Z. Qiao, *J. Am. Chem. Soc.*, 2011, **133**, 20116–20119.
10 J. Mahmood, E. K. Lee, M. Jung, D. Shin, I. Y. Jeon, S. M. Jung, H. J. Choi, J. M. Seo, S. Y. Bae, S. D. Sohn, N. Park, J. H. Oh, H. J. Shin and J. B. Baek, *Nat. Commun.*, 2015, **6**, 6486.
11 B. Xu, H. Xiang, Q. Wei, J. Q. Liu, Y. D. Xia, J. Yin and Z. G. Liu, *Phys. Chem. Chem. Phys.*, 2015, **17**, 15115–15118.
12 F. Li, Y. Y. Qu and M. W. Zhao, *Carbon*, 2015, **95**, 51–57.
13 A. Thomas, A. Fischer, F. Goettmann, M. Antonietti, J. O. Muller, R. Schlogl and J. M. Carlsson, *J. Mater. Chem.*, 2008, **18**, 4893–4908.
14 J. Ortega and O. F. Sankey, *Phys. Rev. B: Condens. Matter Mater. Phys.*, 1995, **51**, 2624–2627.
15 S. H. Zhang, J. Zhou, Q. Wang and P. Jena, *J. Phys. Chem. C*, 2016, **120**, 3993–3998.
16 Y. X. Feng, X. L. Yao, M. Wang, Z. P. Hu, X. G. Luo, H. T. Wang and L. X. Zhang, *J. Chem. Phys.*, 2013, **138**, 164706.
17 J. N. Hart, F. Claeyssens, N. L. Allan and P. W. May, *Phys. Rev. B: Condens. Matter Mater. Phys.*, 2009, **80**, 174111.
18 H. J. Xiang, B. Huang, Z. Y. Li, S. H. Wei, J. L. Yang and X. G. Gong, *Phys. Rev. X*, 2012, **2**, 011003.
19 Z. B. Yan, R. Bi, H. T. Shen, L. Lu, S. C. Zhang and Z. Wang, *Phys. Rev. B*, 2017, **96**, 041103.
20 J. L. Lu, W. Luo, X. Y. Li, S. Q. Yang, J. X. Cao, X. G. Gong and H. J. Xiang, *Chin. Phys. Lett.*, 2017, **34**, 057302.
21 Y. J. Jin, R. Wang, J. Z. Zhao, Y. P. Du, C. D. Zheng, L. Y. Gan, J. F. Liu, H. Xu and S. Y. Tong, *Nanoscale*, 2017, **9**, 13112–13118.
22 S. Barati and S. H. Abedinpour, *Phys. Rev. B*, 2017, **96**, 155150.
23 A. A. Burkov, M. D. Hook and L. Balents, *Phys. Rev. B: Condens. Matter Mater. Phys.*, 2011, **84**, 235126.
24 H. Q. Huang, K. H. Jin and F. Liu, *Phys. Rev. B*, 2017, **96**, 115106.
25 H. Q. Huang and F. Liu, *Phys. Rev. B*, 2017, **95**, 201101.
26 Y. Kim, B. J. Wieder, C. L. Kane and A. M. Rappe, *Phys. Rev. Lett.*, 2015, **115**, 036806.

27 R. Yu, Z. Fang, X. Dai and H. M. Weng, *Front. Phys.*, 2017, **12**, 127202.
28 H. M. Weng, Y. Y. Liang, Q. N. Xu, R. Yu, Z. Fang, X. Dai and Y. Kawazoe, *Phys. Rev. B: Condens. Matter Mater. Phys.*, 2015, **92**, 045108.
29 Y. H. Chan, C. K. Chiu, M. Y. Chou and A. P. Schnyder, *Phys. Rev. B*, 2016, **93**, 205132.
30 R. Yu, H. M. Weng, Z. Fang, X. Dai and X. Hu, *Phys. Rev. Lett.*, 2015, **115**, 036807.
31 Z. Liu, H. Wang, Z. F. Wang, J. Yang and F. Liu, *Phys. Rev. B*, 2018, **97**, 155138.
32 T. Bzdusek, Q. S. Wu, A. Ruegg, M. Sigrist and A. A. Soluyanov, *Nature*, 2016, **538**, 75–78.
33 G. Bian, T. R. Chang, R. Sankar, S. Y. Xu, H. Zheng, T. Neupert, C. K. Chiu, S. M. Huang, G. Q. Chang, I. Belopolski, D. S. Sanchez, M. Neupane, N. Alidoust, C. Liu, B. K. Wang, C. C. Lee, H. T. Jeng, C. L. Zhang, Z. J. Yuan, S. Jia, A. Bansil, F. C. Chou, H. Lin and M. Z. Hasan, *Nat. Commun.*, 2016, **7**, 10556.
34 C. Niu, P. M. Buh, H. Zhang, G. Bihlmayer, D. Wortmann, S. Blügel and Y. Mokrousov, arXiv:1703.05540, 2017.
35 R.-W. Zhang, C.-C. Liu, D.-S. Ma and Y. Yao, arXiv:1710.06267, 2017.
36 P. Zhou, Z. S. Ma and L. Z. Sun, *J. Mater. Chem. C*, 2018, **6**, 1206–1214.
37 H. H. Zhang, Y. Xie, Z. W. Zhang, C. Y. Zhong, Y. F. Li, Z. F. Chen and Y. P. Chen, *J. Phys. Chem. Lett.*, 2017, **8**, 1707–1713.
38 B. Yang, X. M. Zhang and M. W. Zhao, *Nanoscale*, 2017, **9**, 8740–8746.
39 L. H. Li and M. A. N. Araujo, *Phys. Rev. B*, 2016, **94**, 165117.
40 C. W. Niu, P. M. Buhl, G. Bihlmayer, D. Wortmann, Y. Dai, S. Blugel and Y. Mokrousov, *Phys. Rev. B*, 2017, **95**, 235138.
41 B. J. Feng, B. T. Fu, S. Kasamatsu, S. Ito, P. Cheng, C. C. Liu, Y. Feng, S. L. Wu, S. K. Mahatha, P. Sheverdyaeva, P. Moras, M. Arita, O. Sugino, T. C. Chiang, K. Shimada, K. Miyamoto, T. Okuda, K. H. Wu, L. Chen, Y. G. Yao and I. Matsuda, *Nat. Commun.*, 2017, **8**, 1007.
42 C. S. Diercks and O. M. Yaghi, *Science*, 2017, **355**, 923.
43 H. Y. Chen, K. H. Jin, H. Guo, B. J. Wang, A. O. Govorov, X. B. Niu and Z. M. Wang, *Carbon*, 2018, **126**, 480–488.
44 H. P. Wang, W. Luo and H. J. Xiang, *Phys. Rev. B*, 2017, **95**, 125430.
45 S. J. Zhang, C. W. Zhang, S. F. Zhang, W. X. Ji, P. Li, P. J. Wang, S. S. Li and S. S. Yan, *Phys. Rev. B*, 2017, **96**, 205433.
46 T. T. Song, M. Yang, J. W. Chai, M. Callsen, J. Zhou, T. Yang, Z. Zhang, J. S. Pan, D. Z. Chi, Y. P. Feng and S. J. Wang, *Sci. Rep.*, 2016, **6**, 29221.
47 W. X. Ji, B. M. Zhang, S. F. Zhang, C. W. Zhang, M. Ding, P. Li and P. J. Wang, *J. Mater. Chem. C*, 2017, **5**, 8504–8508.
48 B. Wang, S. J. Yuan, Y. H. Li, L. Shi and J. L. Wang, *Nanoscale*, 2017, **9**, 5577–5582.
49 H. J. Yoon, D. H. Jun, J. H. Yang, Z. X. Zhou, S. S. Yang and M. M. C. Cheng, *Sens. Actuators, B*, 2011, **157**, 310–313.
50 A. H. Reshak, S. A. Khan and S. Auluck, *RSC Adv.*, 2014, **4**, 6957–6964.
51 G. Kresse and J. Furthmuller, *Comput. Mater. Sci.*, 1996, **6**, 15–50.
52 J. P. Perdew, K. Burke and M. Ernzerhof, *Phys. Rev. Lett.*, 1996, **77**, 3865–3868.
53 P. E. Blochl, *Phys. Rev. B: Condens. Matter Mater. Phys.*, 1994, **50**, 17953–17979.
54 O. A. Vydrov, J. Heyd, A. V. Krukau and G. E. Scuseria, *J. Chem. Phys.*, 2006, **125**, 074106.
55 S. Grimme, J. Antony, S. Ehrlich and H. Krieg, *J. Chem. Phys.*, 2010, **132**, 154104.
56 A. Togo and I. Tanaka, *Scr. Mater.*, 2015, **108**, 1–5.
57 M. J. Frisch, G. W. Trucks, H. B. Schlegel, G. E. Scuseria, M. A. Robb, J. R. Cheeseman, G. Scalmani, V. Barone, G. A. Petersson, H. Nakatsuji, X. Li, M. Caricato, A. V. Marenich, J. Bloino, B. G. Janesko, R. Gomperts, B. Mennucci, H. P. Hratchian, J. V. Ortiz, A. F. Izmaylov, J. L. Sonnenberg, D. Williams-Young, F. Ding, F. Lipparini, F. Egidi, J. Goings, B. Peng, A. Petrone, T. Henderson, D. Ranasinghe, V. G. Zakrzewski, J. Gao, N. Rega, G. Zheng, W. Liang, M. Hada, M. Ehara, K. Toyota, R. Fukuda, J. Hasegawa, M. Ishida, T. Nakajima, Y. Honda, O. Kitao, H. Nakai, T. Vreven, K. Throssell, J. A. Montgomery Jr, J. E. Peralta, F. Ogliaro, M. J. Bearpark, J. J. Heyd, E. N. Brothers, K. N. Kudin, V. N. Staroverov, T. A. Keith, R. Kobayashi, J. Normand, K. Raghavachari, A. P. Rendell, J. C. Burant, S. S. Iyengar, J. Tomasi, M. Cossi, J. M. Millam, M. Klene, C. Adamo, R. Cammi, J. W. Ochterski, R. L. Martin, K. Morokuma, O. Farkas, J. B. Foresman and D. J. Fox, *Gaussian 16*, Wallingford, CT, 2016.
58 Y. Xu and S. P. Gao, *Int. J. Hydrogen Energy*, 2012, **37**, 11072–11080.
59 M. Mattesini, S. F. Matar and J. Etourneau, *J. Mater. Chem.*, 2000, **10**, 709–713.
60 S. Minami, I. Sugita, R. Tomita, H. Oshima and M. Saito, *Jpn. J. Appl. Phys.*, 2017, **56**, 105102.
61 W. Tang, E. Sanville and G. Henkelman, *J. Phys.: Condens. Matter*, 2009, **21**, 084204.
62 H. Takeda, T. Takashima and K. Yoshino, *J. Phys.: Condens. Matter*, 2004, **16**, 6317–6324.
63 M. Phillips and V. Aji, *Phys. Rev. B: Condens. Matter Mater. Phys.*, 2014, **90**, 115111.
64 C. Fang, H. M. Weng, X. Dai and Z. Fang, *Chin. Phys. B*, 2016, **25**, 117106.
65 W. Chen, H. Z. Lu and J. M. Hou, *Phys. Rev. B*, 2017, **96**, 041102.
66 P. Y. Chang and C. H. Yee, *Phys. Rev. B*, 2017, **96**, 081114.
67 R. Bi, Z. B. Yan, L. Lu and Z. Wang, *Phys. Rev. B*, 2017, **96**, 201305.
68 K. H. Michel and B. Verberck, *Phys. Rev. B: Condens. Matter Mater. Phys.*, 2009, **80**, 224301.
69 F. Mouhat and F. X. Coudert, *Phys. Rev. B: Condens. Matter Mater. Phys.*, 2014, **90**, 224104.
70 Q. Wei and X. H. Peng, *Appl. Phys. Lett.*, 2014, **104**, 251915.
71 X. D. Zhou, W. X. Feng, S. Guan, B. T. Fu, W. Y. Su and Y. G. Yao, *J. Mater. Res.*, 2017, **32**, 2993–3001.
72 J. Mahmood, F. Li, S. M. Jung, M. S. Okyay, I. Ahmad, S. J. Kim, N. Park, H. Y. Jeong and J. B. Baek, *Nat. Nanotechnol.*, 2017, **12**, 441–446.